Journal of Theoretical and Applied Information Technology
15th January 2025. Vol.103. No.1

ISSN: 1992-8645 www.jatit.org E-ISSN: 1817-3195

# A HYBRID QUANTUM-INSPIRED CNN ARCHITECTURE FOR EFFICIENT AND ACCURATE BRAIN TUMOR CLASSIFICATION WITH EXPLAINABILITY ANALYSIS

**SHEETHAL M. S[1]*, DR. P. AMUDHA[2]**
[1]*Department of Computer Science and Engineering
Avinashilingam Institute for Home Science & Higher Education for Women
Coimbatore, Tamil Nadu, 641017, India
[1]*sheethalbasil@gmail.com
[2]Department of Computer Science and Engineering
Avinashilingam Institute for Home Science & Higher Education for Women
Coimbatore, Tamil Nadu, 641017, India
[2]amudha_cse@avinuty.ac.in

**ABSTRACT**

Brain tumors are considered one of the serious types of cancer and catching them early is crucial for better patient results. The use of Magnetic Resonance Imaging (MRI) plays a role in spotting and categorizing brain tumors; however, it can be tough and time consuming for radiologists to interpret these images. To address this issue, this study introduces a Quantum Inspired Convolutional Neural Network (QCNN) that integrates concepts from quantum mechanics, such as superposition and entanglement, with traditional Convolutional Neural Network (CNN) architectures. This innovative approach enhances feature extraction capabilities, allowing the model to recognize intricate patterns within MRI images more effectively. The QCNN achieved impressive results, reaching a peak validation accuracy of 99.44% and demonstrating significantly improved classification for various types of brain tumors, including Glioma and Meningitis. These findings highlight the potential of the QCNN framework to revolutionize tumor detection, offering radiologists a powerful tool that enhances diagnostic accuracy and efficiency in clinical practice, ultimately leading to better patient care and outcomes in the medical imaging field.
**Keywords:** *Quantum, CNN, Architecture, Brain Tumor, Classification*

## 1. INTRODUCTION

Brain tumors are considered to be one of the serious and life-threatening types of cancer worldwide [1]. They consist of malignant growths such as gliomas and meningiomas that differ in aggressiveness and prognosis [2]. Detecting such tumors on and accurately identifying them are crucial for effective treatment due, to their ability to impact vital neurological functions. Detecting brain tumors at a stage can greatly enhance the chances of survival by allowing for prompt surgical procedures or treatments like radiation therapy and chemotherapy [3]. It is crucial to differentiate between types of brain tumors such as benign and malignant since this helps in devising the right treatment plan accordingly. However classifying brain tumors accurately is quite challenging due to the structure of the brain the diverse manifestations of tumors and the similarities in characteristics, among different tumor varieties [4].

Magnetic Resonance Imaging (MRI) a choice for diagnosing brain tumors due to its high contrast resolution and detailed soft tissue images that are essential, for tumor visualization purposes. MRI provides a range of imaging techniques like T1 weighted and T2 sequences along with FLAIR to highlight various tissue characteristics that help in pinpoint the boundaries of tumors and detect infiltration as well as surrounding edema [5]. Even though MRI has its advantages in medical imaging interpretation; understanding MRI images is often a time-consuming task that demands specialized radiological knowledge and expertise. To make a diagnosis, radiologists must review several MRI slices from various angles, record the sequences employed, and evaluate minute differences in tissue properties [6]. It takes a long time to utilize this approach. This approach can vary depending on how each individual interprets it, as different people hold different ideas. Moreover, the growing amount of imaging data produced in settings intensifies the workload for radiologists increasing the chance of mistakes in diagnoses or delays in identification [2]. These obstacles highlight the necessity, for fast automated solutions to support the identification and categorization of brain tumors. Systems like these could enhance the skills of radiologists by

offering quick evaluations of MRI images. The progress in intelligence (AI) and deep learning has paved the way, for creating such automated systems [7]. Through the use of datasets and advanced algorithms AI driven tools are able to identify characteristics and patterns linked to various brain tumors. This process greatly assists in their identification and categorization [8].

Deep learning techniques like Convolutional Neural Networks (CNN) have transformed medical image analysis by excelling in tasks such as segmentation and detection and by recognizing patterns related to various medical conditions from pixel level data [9]. Their success in tasks, like tumor detection and organ segmentation has often surpassed image processing methods. CNNs main advantage is their capability to grasp levels of abstract feature representations by using convolutional layers in a stacked manner [10, 11]. The initial layers can identify features like edges and textures whereas the later stages focus on recognizing intricate patterns like shapes and objects. This hierarchical learning approach empowers CNN to perform well in tasks such as image classification that necessitate the differentiation of subtle distinctions, between different categories [12]. CNN networks are extensively used in imaging because of their capacity to process vast datasets and adapt effectively to various types of imaging such as MRI scans and ultrasounds [13]. For instance, in identifying types of brain tumors from MRI scans for accurate diagnoses [14] CNN networks have proven helpful, to radiologists; despite this benefit conventional CNN structures encounter challenges when dealing with intricate medical images. Medical images frequently display patterns and nuanced differences that traditional CNN models might not capture entirely accurately. Additionally, CNN models heavily lean on spatial hierarchies and localized patterns which might not be comprehensive enough to identify intricate relationships and dependencies across various parts of the image [15].

In recent years, quantum-inspired principles, particularly entanglement and superposition, have shown promise in overcoming the limitations of traditional deep learning methods. These principles, rooted in quantum mechanics, offer new avenues for feature extraction and pattern recognition that are especially valuable in medical imaging, where subtle differences in complex images play a critical role in diagnosis. Incorporating quantum inspired ideas is crucial here. Key principles such as entanglement and superposition from quantum mechanics can actually boost how deep learning models extract features and recognize patterns [16]. In the realm of quantum physics entanglement deals with the connection, between quantum states that can represent relationships not easily captured using traditional approaches [17]. This concept, when adapted into neural networks, enables models to capture **dependencies and relationships between distant regions** in an image, which is crucial for identifying patterns across diverse areas of MRI scans. In conventional CNNs, such relationships are often challenging to capture, as they primarily rely on localized filters that may miss broader connections within the image. On the hand superposition allows for exploring multiple scenarios simultaneously potentially enhancing a model's capacity to generalize across various patterns in medical images [18]. This enables the network to consider multiple potential interpretations of complex patterns, which is particularly beneficial in distinguishing between similar-looking structures in brain images. By incorporating this quantum inspired concepts into CNN designs scientists seek to surpass the constraints of CNN models. For instance, quantum inspired CNN models may enhance their ability to capture both overall characteristics by utilizing entanglement to depict connections among various sections of the picture [19]. This upgraded feature extraction could result in enhanced precision in healthcare image examination assignments in situations where slight distinctions hold significant importance, for diagnosis. Moreover, the quantum inspired method could bring about a degree of parallelism in calculations akin to quantum superposition enabling the network to handle various hypotheses all at once [20]. This could lead to convergence in training and more effective exploration of potential solutions, in complex medical image tasks ultimately boosting the model's performance.

In tackling the issue of identifying brain tumors in intricate medical images this article presents a novel Quantum Inspired Convolutional Neural Network (QCNN) structure that merges quantum computing concepts with the conventional CNN framework. The goal is to enhance the efficiency of automated brain tumor detection systems by combining quantum inspired layers with CNN layers in the QCNN model to detect complex features and connections, in multi-modality MRI images more effectively.

The main contributions of the proposed Quantum Convolutional Neural Network (QCNN) model for brain tumor classification:

- Integration of Quantum Principles: Incorporates quantum principles like superposition and entanglement, known to enhance pattern recognition, to improve the learning process for more effective analysis of image details.
- Enhanced Precision in Tumor Classification: Aims to achieve higher accuracy in distinguishing between healthy and abnormal tissues, improving identification of different brain tumor types.
- Improved Feature Extraction: Enhances feature extraction capabilities, allowing the model to better capture and analyze critical details in MRI data.
- Greater Generalization Ability: Increases the model's ability to generalize across different MRI data types, ensuring robustness across various datasets.
- Reduced Risk of Misidentification: Provides reliable performance, lowering the chances of misidentification through improved accuracy and generalization.
- Efficiency in Computational Resources: Quantum-inspired methods reduce computational load, making the QCNN model more resource-efficient when processing complex and large MRI datasets.
- Enhanced Processing Speeds: Enables faster processing, which is critical for clinical applications where prompt diagnosis is essential.
- Suitability for Clinical Applications: The QCNN's efficiency and precision make it highly suitable for use in clinical environments, supporting quick and accurate diagnoses of brain tumors.

Ultimately, the introduction of the QCNN architecture in brain tumor detection aims to contribute to better patient outcomes by providing more accurate and reliable diagnostic tools. The rest of the article has been organized as follows. Section II discussing the related works focusing on Machine learning and Deep Learning in Brain Tumor Detection, Challenges in Conventional CNN Architectures and Quantum-Inspired Approaches. Section III discussing the proposed methodology using quantum inspired concepts. Section IV analyzing the results of the proposed method with explainability analysis and finally section V concludes with the results obtained and future aspects of the proposed method.

## 2. RELATED WORKS

### 2.1. Machine learning and Deep Learning in Brain Tumor Detection

In this section, we discuss the various ways machine learning and deep learning have been applied to studying infectious brain tumors and interpreting medical images. Over the past two decades, medical image analysis has attracted a lot of attention and research interest because of the wide range of uses it offers in healthcare, particularly in the investigation and diagnosis of patients. In order to classify brain images and analyze brain architecture, studies suggest machine learning-based strategies [21]. Abd-Ellah et al. [22] conducted an in-depth study of the available methods for diagnosing brain MRI scans, comparing and contrasting the strengths and weaknesses of traditional machine learning and deep learning approaches. Additionally, the authors presented a new semi-automatic segmentation approach for images of brain tumors [23]. For 3D MRI segmentation, this model made use of a T1W configuration. Another CNN-based architecture was presented for breast cancer picture categorization [24]. This system's maximum accuracy for tumor segmentation and localization was due to its architectural design, which extracted data from fitting scales. Additionally, a CNN-based model for diagnosing brain tumors used GoogLeNet, InceptionV3, DenseNet201, AlexNet, and ResNet50 [25]. The results indicated that the proposed method was able to detect and categorize cancers in MR images with high precision. Overall, the corpus of work shows substantial advancement in segmenting and classifying brain tumors from MRI scans, as well as their 3D visualization. However, there is still a requirement for innovative methodologies to increase the efficacy of feature extraction, tumour classification, and localization.

### 2.2. Challenges in Conventional CNN Architectures

For image recognition, several CNN models, such as AlexNet [26], GoogleNet [27], and ResNet [28], have been trained on large datasets like ImageNet. Afterward, these models can be applied to different tasks without requiring additional training. Furthermore, aside from a few learned features, the weights remain unchanged. These models are particularly useful when data samples are limited. There are several reasons for using pre-trained models. First, training large models on enormous datasets requires significant computational power. Second, training such models can take weeks or even months. Lastly, a pre-trained model can accelerate convergence and improve network generalization. Training deep learning (DL) methods requires a vast number of

images, but achieving high performance in such cases can be challenging. When large datasets are available, deep convolutional neural networks (DCNNs) with multiple layers can produce excellent results in image classification or recognition tasks, sometimes even surpassing human performance [29]. However, to avoid overfitting, both large datasets and well-generalizing DCNN models are essential in these applications. There is no strict lower limit on dataset size when training a DCNN model. However, when smaller datasets are used for training, overfitting or underfitting issues arise, especially with models that have fewer layers, resulting in inadequate accuracy. Models with fewer layers perform poorly because they cannot leverage the hierarchical features present in large datasets. Acquiring sufficient training data for deep learning models is a significant challenge. For example, obtaining labeled datasets is particularly expensive in fields like environmental science and medical imaging. CNN models trained on the ImageNet dataset, which contains natural images, are often used to enhance performance in medical image classification. However, these natural images differ significantly from raw medical images, limiting improvements in model performance. Additionally, lightweight models trained from scratch often outperform conventional ImageNet-transferred models, highlighting that transfer learning (TL) from unrelated domains may not enhance performance in medical imaging tasks [30]. Therefore, in some cases, using pre-trained models may not be a cost-effective solution. In 2020, a few researchers successfully employed same-domain TL, reporting excellent results [31, 32].

### 2.3. Quantum-Inspired Approaches

Gonaygunta et al. [33] introduced quantum-inspired algorithms for pattern recognition, laying the groundwork for quantum-enhanced deep learning models. Shi et al. [34] and Fan et al. [35] developed a quantum-inspired neural network, demonstrating the potential benefits of quantum principles like entanglement and superposition in enhancing feature extraction and improving model performance. This work provides a direct link to the concept of quantum-inspired CNNs. The major challenges in quantum-inspired models can introduce additional complexity in their design and implementation. This can make them harder to understand and optimize compared to traditional models, potentially hindering their adoption in practical applications [36]. Many quantum-inspired algorithms do not scale well with increasing data size or complexity. This can limit their effectiveness in large-scale applications where traditional deep learning models excel [37]. While quantum-inspired methods often promise improved performance through principles like entanglement and superposition, empirical evidence is sometimes inconclusive, and the performance gains over classical methods can vary significantly depending on the specific application and implementation [38].

## 3. METHODOLOGY

The new Quantum Inspired CNN design depicted in figure 1 brings changes to the standard CNN layout by integrating concepts inspired by quantum mechanics. These adjustments are geared towards improving the model's capacity to recognize patterns and relationships within MRI data, for more precise tumor classification.

### 3.1 Data Preprocessing and Augmentation:

The input dataset used in this study consists of brain tumor MRI images, resized to standardized dimensions of 128×128 pixels with three color channels (128×128×3) to ensure consistency across the dataset. To improve the model's generalization capabilities and mitigate overfitting, extensive data augmentation techniques are applied. This augmentation process includes random rotations within a specified degree range and horizontal and vertical shifts, allowing the model to encounter varied perspectives of the same image. These augmented images effectively increase the diversity of the dataset, helping the model learn more robust features representative of brain tumor patterns. During training, the augmented images are organized into mini-batches of 32, ensuring an efficient and stable learning process while optimizing computational resources.

### 3.2 Initial Layers (Convolution and Pooling)

The architecture begins with standard convolutional layers that extract features from the input MRI images. These features are representations of edges, textures, and other important structures in the images. The layers typically consist of convolution operations followed by non-linear activation functions and pooling operations to reduce the spatial dimensions. The convolution operation involves applying a set of filters (or kernels) to the input image to produce feature maps. Mathematically, this is expressed as:

$$F_{i,j}^{k} = (X * W^{k})_{i,j} + b^{k} \quad (1)$$

Where $X$ is the input image, $W^{k}$ is the k-th filter, $b^{k}$ is the bias term for the k-th filter, $F_{i,j}^{k}$ is the resulting feature map at position (i,j). Pooling layers downsample the feature maps, reducing their dimensions while preserving important features. This operation is crucial for reducing computational complexity and avoiding overfitting.

### 3.3 Quantum Convolution and Addition

#### *3.3.1 Quantum-Inspired Layer*

In classical CNN architectures, the ability to recognize complex patterns is primarily driven by spatial hierarchies formed through convolutional layers and local feature extraction. However, this structure may overlook subtle global dependencies and intricate relationships within data, which are especially significant in medical imaging tasks such as brain tumor classification. Quantum mechanics introduces powerful principles—superposition and entanglement—that can address these limitations by enabling a more holistic, interconnected understanding of image data.

#### *3.3.2 Quantum Superposition and Feature Combination*

In quantum physics superposition denotes the capacity of a quantum system to be present in states, at the same time. Similarly in the quantum inspired layer the feature maps derived from the layers are merged in a way that enables the model to investigate numerous feature combinations concurrently. For instance, when we possess two feature maps labeled as $F_1$ and $F_2$ the quantum inspired amalgamation can be represented as:

$$F_{super} = \alpha F_1 + \beta F_2 \quad (2)$$

where α and β are coefficients that determine the contribution of each feature map. This resembles the principle of quantum superposition, where different states contribute to the overall system.

In QCNN, feature maps from convolutional layers are combined in a manner that allows simultaneous consideration of multiple feature interactions. This enables the network to learn more complex patterns in MRI images helping to identify subtle yet diagnostically significant variations across different tumor types.

In conventional CNNs, feature maps are processed sequentially, limiting combinations primarily to spatial hierarchies. However, with superposition, the network can explore a range of potential feature relationships concurrently, enhancing the model's ability to learn complex, nuanced patterns. This approach can capture subtle but diagnostically critical variations in MRI images, such as minor changes in tumor shape or texture, by allowing the model to investigate multiple feature interactions at once.

#### *3.3.3Quantum Interference and Convolution with Small Kernels*

Quantum interference refers to the phenomenon where the probability amplitude of quantum states can add or subtract, leading to constructive or destructive interference. This concept is mimicked in the architecture by using small convolutional kernels (1x1 convolutions) that focus on fine-grained details of the feature maps. The 1x1 convolution operation is defined as:

$$F'_{i,j} = W_{1x1} \cdot F_{i,j} + b_{1x1} \quad (3)$$

Where $W_{1x1}$ is the weight matrix of the 1x1 convolution filter, $F_{i,j}$ is the input feature map, $F'_{i,j}$ is the output feature map after the 1x1 convolution. This operation allows the network to emphasize specific fine details within the feature maps, similar to how quantum interference can highlight or suppress certain quantum states.

#### *3.3.4 Addition Layer and Quantum Entanglement*

Quantum entanglement allows for the correlation of states across different regions which translates in QCNN to the ability to capture dependencies across spatially separated features. This property is crucial in medical imaging where identifying diffuse patterns and relationships across different regions in an MRI can greatly impact diagnosis. This entanglement inspired layers help the model grasp these non-local connections improving its overall classification capability. In the CNN architecture, this concept is loosely mimicked by an addition layer that combines outputs from different pathways within the network. For instance, if two pathways produce outputs $P_1$ and $P_2$, the addition layer computes:$P = P_1 + P_2$. This operation integrates information from different parts of the network, allowing the architecture to capture complex dependencies between features, similar to quantum entanglement.

In MRI-based brain tumor detection, entanglement allows the network to model relationships between distant parts of the image, vital for detecting diffuse patterns or spread in tumor regions. By capturing these complex dependencies, the network gains the capacity to detect subtle and spatially dispersed features that signify tumor presence, leading to improved classification performance.

### 3.4 Deeper Layers and Final Classification

After the quantum-inspired layer, the architecture continues with deeper convolutional and fully connected layers, which further process the combined features. The final layer is a softmax layer that outputs the probabilities for each tumor class. The fully connected (FC) layer aggregates the features extracted by the previous layers and makes the final prediction. It is mathematically represented as: $y = \sigma(W_{FC} \cdot F_{final} + b_{FC})$ (4)

Where $W_{FC}$ and $b_{FC}$ are the weights and biases of the FC layer, and σ is the softmax function that converts the outputs into probabilities.

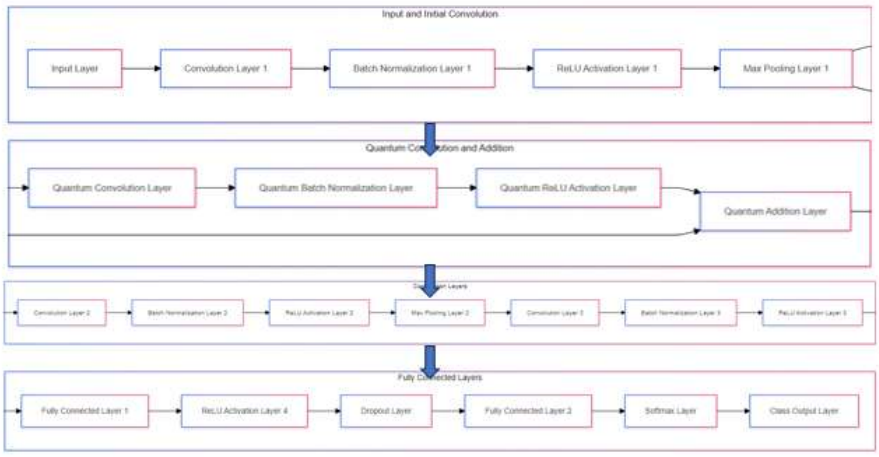


*Figure 1 The Quantum Cnn Architecture*

#### *3.4.1. Quantum CNN flow structure*

The flowchart shown in figure 2 illustrates the step-by-step procedure for setting up a Quantum Inspired Convolutional Neural Network to detect brain tumors effectively. To kick start the process; MRI data is first loaded and undergone preprocessing to normalize and refine the images for input, into the network. After this stage, the data is split into training and validation sets to enable precise assessment of the model's performance as it progresses. Once the data has been divided into sections and the image to be entered into the system is resized to comply with the CNN design parameters. The layers and components that will form the network's basis are outlined in detail in this part of the procedure, which describes the CNN structure. Feature extraction inspired by quantum mechanics is then integrated into the architecture. After that, the network is assessed to ensure that the components inspired by quantum mechanics are functioning correctly within the CNN framework.

The training process begins once the network is configured and ready. Each time a new epoch begins the network undergoes training while adjusting the learning rate to enhance its performance whenever necessary. Following that phase, the model gets evaluated using the validation set to determine how accurate it is. In case the model's accuracy shows improvement, the best version of it is saved and updated; if not the training proceeds with adjustments and fine tuning, for better results. After selecting the optimal model, a confusion matrix is generated to evaluate the classification performance for each category. Following this assessment, ROC curves are utilized to evaluate the networks capability to differentiate among tumor types. The last step consists of preserving the model and finalizing the training procedure. This process covers the path from preparing the data to developing the final trained model. It highlights how utilizing quantum inspired layers can enhance feature extraction and boost the accuracy of brain tumor classification.

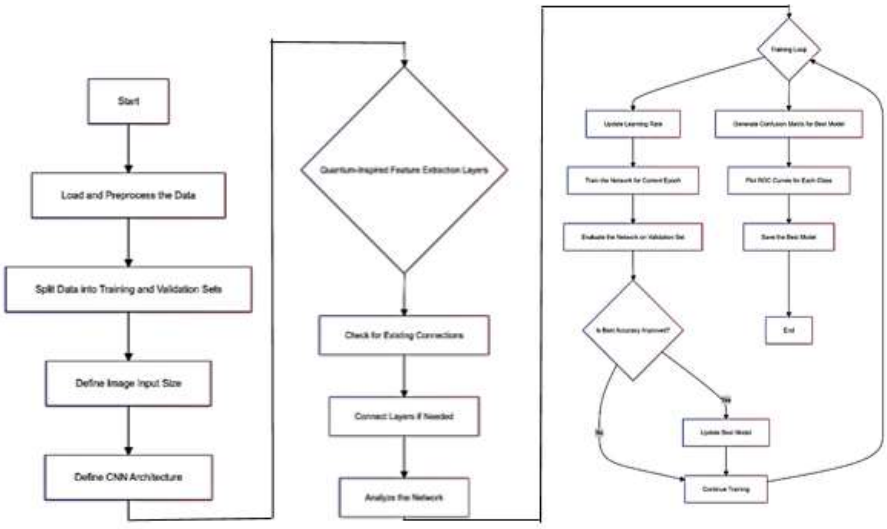


*Figure 2: Quantum CNN Flow Structure*

### *3.4.2. Quantum-Inspired Learning Rate*

The Quantum Inspired Learning Rate introduces a method that utilizes concepts from quantum mechanics to adapt the learning rate in real time during training sessions. The idea takes inspiration from the nature of quantum mechanics and often employs functions like sine and cosine to mimic the oscillating motions of quantum states in models. The learning rate in this approach is adjusted using a cosine function that varies the rate between a peak and a minimum level, throughout the training sessions. This is mathematically represented by the following equation:

$$lr(epoch) = \max\left(10^{-6}\frac{10^{-4}\times\left(1+c\ \left(\frac{\pi\times epoc}{maxEpochs}\right)\right)}{2}\right) \quad (5)$$

The cosine function within the equation models a smooth, periodic decay of the learning rate over time. The argument of the cosine function is:

$$\frac{\pi\times epoch}{maxEpochs} \quad (6)$$

This term ensures that the cosine function completes half of its period over the total number of training epochs (maxEpochs). The learning rate starts at its maximum value and decreases smoothly to its minimum value as training progresses.

*Table 1: Learning Rate Formula Components*

| **Components** | **values** |
|---|---|
| epoch | 10 |
| maxEpochs | 10 |
| The initial maximum learning rate | $10^{-4}$ |
| The minimum allowable learning rate | $10^{-6}$ |

Cosine Function Scaling*: Cosine Function Scaling produces a value that oscillates smoothly* between 0 and 1 as epoch progresses from 0 to maxEpochs. This term modulates the learning rate, starting from its maximum value (when epoch = 0 and cosine is 1) and decreasing it gradually to its minimum value (when epoch = maxEpochs and cosine is -1).

$$\text{Cosine Function Scaling} = \frac{1+\cos\left(\frac{\pi\times epoch}{maxEpoch}\right)}{2} \quad (7)$$

*Dynamic Range Control:* The entire expression is multiplied by $10^{-4}$ as shown in Table 1, setting the initial learning rate. The max function ensures that the learning rate does not fall below a defined minimum threshold of $10^{-6}$, preventing the learning rate from becoming too small, which might slow down the convergence excessively or lead to premature stagnation.

*Intuition Behind Quantum-Inspired Learning Rate:* The application of a cosine function mirrors the undulating patterns seen in quantum phenomena; wherein probabilities fluctuate and may interact positively or negatively with each other. Similarly, through the implementation of a cosine schedule the learning rate fluctuates enabling the model to investigate areas of the loss landscape in greater depth. The recurring rise and fall in the learning rate assist the model, in steering of becoming trapped in local minimum points. Occasionally boosting the learning rate can nudge the model away from a low

point and enable it to delve into a wider range of parameter options in search of a superior overall solution. The gradual decrease in the learning rate guarantees that as the model nears convergence the adjustments it makes become finer tailoring and reducing losses with precision. The quantum inspired approach to adjusting the learning rate proves beneficial, in complex deep learning setups where the loss terrain is intricate and filled with numerous smaller low points. By adapting the learning rate as needed in time this technique effectively manages the tradeoff between exploring new possibilities (with higher learning rates) and leveraging existing knowledge (with lower learning rates) leading to effective and smooth training processes.

## 4. RESULTS AND DISCUSSION

### 4.1. Dataset used for proposed model analysis

*Table 2: Dataset 1 [45-47] Details On Brats 2019 & 2020*

| Class | Number of Images |
|---|---|
| Ependimoma T1 | 70 |
| Ganglioglioma T1 | 20 |
| Glioblastoma T1 | 90 |
| Medulloblastoma T1 | 26 |
| Oligodendroglioma T1 | 152 |
| Schwannoma T1 | 276 |

*Table 3: Dataset 2 Based On [39]*

| Class | Number of Images |
|---|---|
| Glioma Tumor | 1427 |
| Meningioma Tumor | 708 |
| No Tumor | 1500 |
| Pituitary Tumor | 930 |

The proposed model analysis utilizes two datasets for evaluating tumor classification performance: Dataset 1 [42-44], which includes details on the BraTS 2019 & 2020 dataset, and Dataset 2, which offers is based on [39] which was acquired from Nanfang Hospital, Guangzhou, China, and General Hospital, Tianjing Medical University, China. Dataset 1, presented in Table 2 and figure 3, provides a diverse array of brain tumor images from the BraTS 2019 & 2020 datasets. The table reveals six specific tumor types, with varying sample sizes. Schwannoma T1 represents the largest class with 276 images, while Ganglioglioma T1 has the fewest, with only 20 images. Glioblastoma T1, another prominent tumor type, is represented by 90 images, making it a key focus for model training. Ependimoma T1 and Medulloblastoma T1, with 70 and 26 images respectively, provide additional variety and challenge to the dataset. The largest group, Oligodendroglioma T1, contains 152 images, offering a considerable volume for analyzing this particular tumor type. This dataset is significant for evaluating the model's ability to handle both abundant and sparse classes, simulating real-world scenarios where certain tumor types are more prevalent than others. Dataset 2 [36], outlined in Table 3 and figure 4, is from the BraTS-2020 dataset, which offers a larger and more balanced set of tumor and non-tumor images, focusing on four major categories. The No Tumor class has the highest number of images at 1,500, indicating its critical role in ensuring the model can differentiate between healthy and diseased brain scans. Glioma Tumor, with 1,427 images, and Meningioma Tumor, with 708 images, are well-represented, ensuring the model has sufficient data to learn from these common tumor types. The Pituitary Tumor class, though smaller with 940 images, still provides a significant number of examples for analysis. The inclusion of a large number of images across multiple classes in this dataset enhances the robustness of the model and improves its capacity to generalize across different types of brain abnormalities.

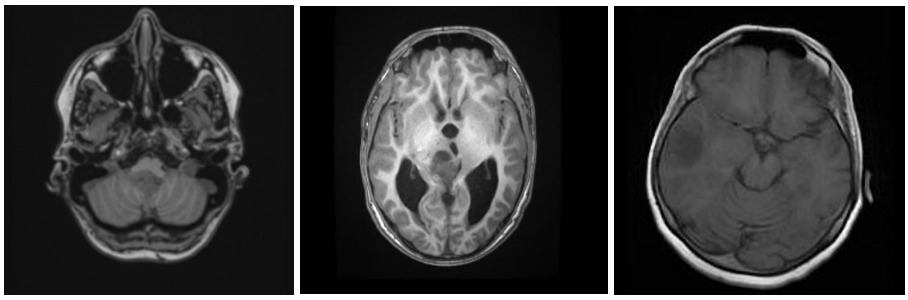

(a) (b) (c)

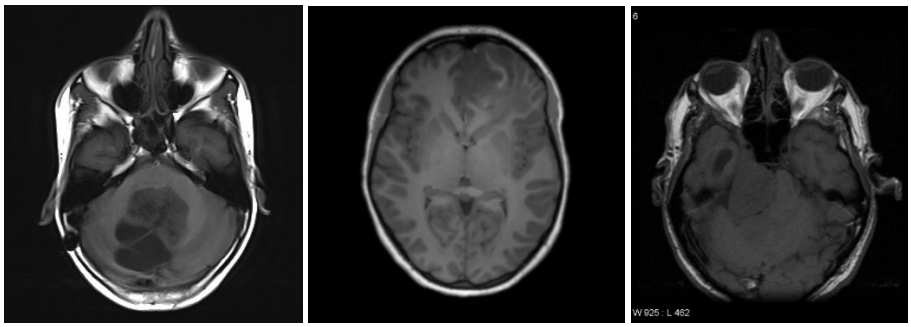

(d) (e) (f)

*Figure 3: Samples Of Dataset 1 By Brats 2019 & 2020 [42-44] (A) Ependimoma T1 (B) Ganglioglioma T1 (C) Glioblastoma T1 (D) Medulloblastoma T1 (E) Oligodendroglioma T1 (F) Schwannoma T1*

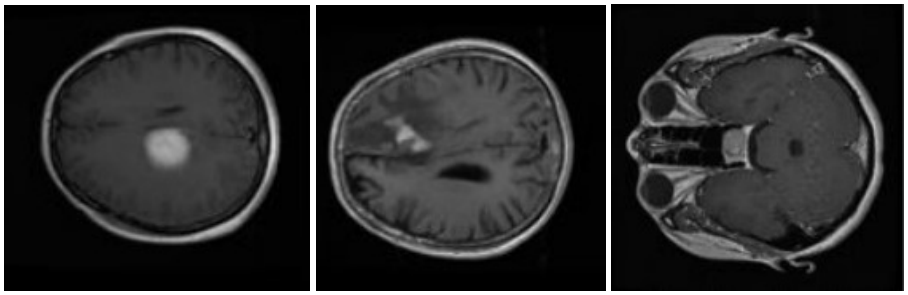

(a) (b) (c)

*Figure 4: Samples Of Dataset 2 Provided By Cheng Et. Al. [36] (A) Meningioma Tumor (B) Glioma Tumor (C) Pituitary Tumor*

*Training Trials for dataset 1:* The model was trained using a hybrid architecture that combines classical and quantum-inspired convolutional layers. The training process employed a cosine annealing learning rate schedule, inspired by quantum mechanical principles, which helps dynamically adjust the learning rate, allowing the model to explore different parameter spaces more effectively and avoid local minima. The training was conducted over multiple epochs as shown in Table 2. Early stopping was applied to prevent overfitting, ensuring that training would halt if the model's performance on a validation set stopped improving. A moderate batch size was chosen to balance the computational efficiency and generalization capability. Adam Optimizer were utilized to adjust the weights in the neural network, while regularization techniques, such as dropout, were employed to prevent overfitting.

**Table 4:** Validation Accuracy and Learning Rate across Trials

| Trial | Learning Rate | Validation Accuracy (%) |
|---|---|---|
| 1 | 9.0451E-05 | 95.24 |
| 2 | 9.7553E-05 | 95.81 |
| **3** | **7.9389E-05** | **97.62** |
| 4 | 6.5451E-05 | 93.65 |
| 5 | 5.0000E-05 | 96.03 |
| 6 | 3.4549E-05 | 94.44 |
| 7 | 2.0611E-05 | 96.83 |
| 8 | 9.5492E-05 | 96.83 |
| 9 | 2.4472E-05 | 92.86 |
| 10 | 1.0000E-06 | 84.13 |

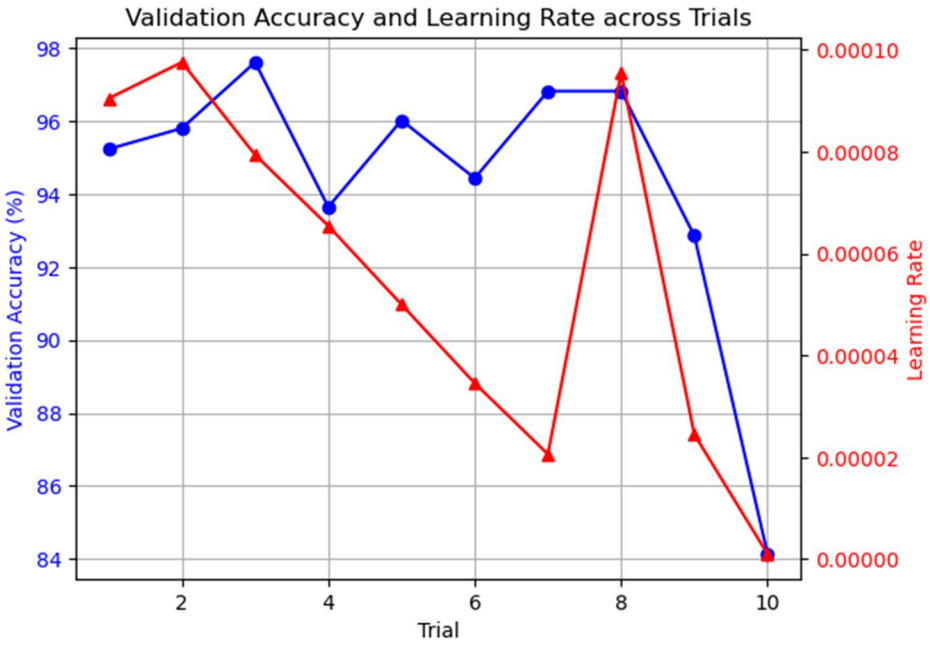


*Figure 5: Validation Accuracy And Learning Rate Across Trials*

The table 4 and figure 5 presents the results of various trials during the training of a hybrid architecture that combines classical and quantum-inspired convolutional layers. The training employed a cosine annealing learning rate schedule**,** which is designed to dynamically adjust the learning rate, mimicking principles from quantum mechanics to explore parameter spaces more effectively and avoid local minima. The cosine annealing schedule helps adjust the learning rate throughout training, and the table reflects the impact of these adjustments on validation accuracy. Trials with higher validation accuracy likely benefited from optimal learning rates at key points during training, enabling the model to escape local minima and converge more effectively. In Trial 3, with a learning rate of $7.9389 \times 10^{-05}$, achieved the highest validation accuracy of 97.62%. This suggests that the cosine annealing schedule allowed the model to find an effective learning rate that enabled robust feature extraction, particularly in a complex architecture combining classical and quantum-inspired layers. Early stopping was used to prevent overfitting, which is evident from the moderate-to-high validation accuracy across most trials. The table shows that the model consistently avoided overfitting, as seen in Trials 2, 5, and 7, where validation accuracies remained high (95.81%, 96.03%, and 96.83%, respectively). This indicates that the training process effectively halted before performance on the validation set could degrade. rials with lower validation accuracy, such as Trial 10 (84.13%) with a very low learning rate of $1.0000 \times 10^{-06}$, suggest that the learning rate was too small for effective training. The cosine annealing schedule might have reduced the learning rate too much, hindering the model's ability to adjust weights sufficiently, leading to slower convergence or suboptimal solutions. The use of a moderate batch size likely helped strike a balance between computational efficiency and the model's ability to generalize, as reflected in the relatively high validation accuracies across different learning rates. Regularization techniques, like dropout, contributed to preventing overfitting, particularly in trials with higher learning rates where the risk of overfitting might have been more significant. The consistency in validation accuracy (above 92% in most trials) suggests that these techniques effectively stabilized the training process.

*Table 5: Performance Metrics*

| Class | Accuracy | Precision | Recall | F1-Score | Specificity | AUC |
|---|---|---|---|---|---|---|
| Ependimoma T1 | 0.992 | 1.000 | 0.928 | 0.963 | 1.000 | 0.97 |
| Ganglioglioma T1 | 1.000 | 1.000 | 1.000 | 1.000 | 1.000 | 1.00 |
| Glioblastoma T1 | 0.992 | 1.000 | 0.944 | 0.971 | 1.000 | 1.00 |
| Meduloblastoma T1 | 1.000 | 1.000 | 1.000 | 1.000 | 1.000 | 1.00 |
| Oligodendroglioma T1 | 1.000 | 1.000 | 1.000 | 1.000 | 1.000 | 1.00 |
| Schwannoma T1 | 0.984 | 0.965 | 1.000 | 0.982 | 0.971 | 1.00 |

The table 5 presents performance metrics for different brain tumor types, indicating how well the model performed across various evaluation criteria. The high accuracy scores nearing 1 for each class indicate the model's capability, in accurately recognizing different types of tumors very effectively. Recall, which measures the model's ability to identify all actual cases of a tumor type, is slightly lower for Ependimoma T1 (0.928) and Glioblastoma T1 (0.944). This suggests that while the model performs exceptionally well overall, it misses a small number of true positive cases for these specific tumor types. The F1-Score, which balances precision and recall, also reflects this trend, with slightly lower values for Ependimoma T1 (0.963) and Glioblastoma T1 (0.971), although the scores remain high across all classes. Specificity, which measures the model's ability to correctly identify non-tumor cases or distinguish between different tumor types, is perfect (1.000) for all classes, indicating that the model effectively avoids false negatives. Lastly, the AUC scores, with most classes achieving a score of 1.00, suggest that the model has an excellent ability to distinguish between classes. Overall, the table highlights the robustness of the model across various metrics, with only minor variations in recall and F1-Score for certain tumor types.

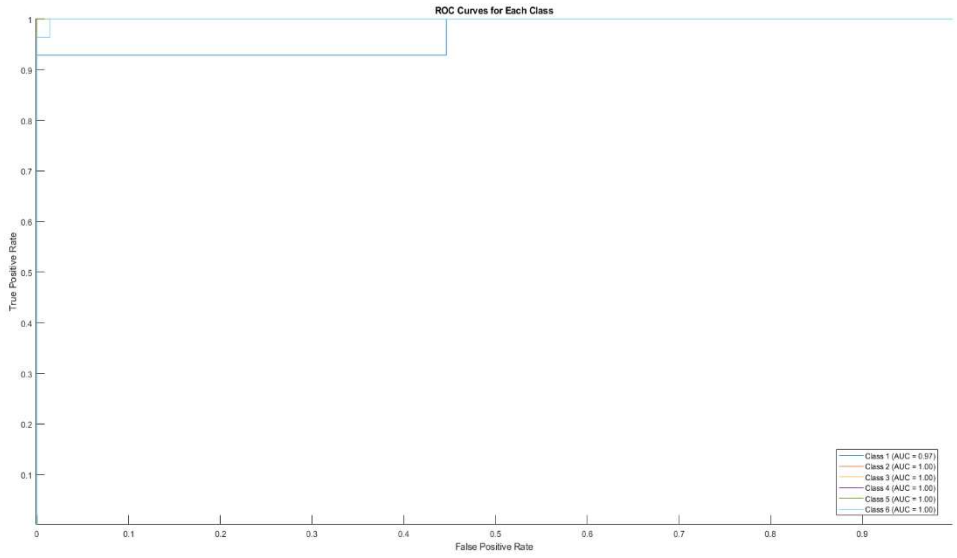


*Figure 6: ROC curve on proposed model in dataset 1*

The ROC curve shown in Figure 6 for each class demonstrates accurate classification performance with close to perfect AUC values shown under the curve for most tumor types except Ependymoma Tumor 1 which shows an AUC value of 0.97 indicating the classifiers outstanding discrimination ability with just a slight margin of imperfection, in classification. The ROC curve of Ependymoma

Tumor 1 shows a shift away from the upper left corner indicating a slightly elevated false positive rate compared to other types of tumors. This aligns with the recall rate of 92% and F1- score of 96% for this category as seen in the table 5; these values are slightly lower than those, for the other categories. The ROC curves of Ganglioglioma T1 differ significantly from those of Glioblastoma T1 and Medulloblastoma T1 due to the characteristics of each tumor type observed in their precision recall and sensitivity specificity values being close, to 100%.

Training Trials for dataset 2

The table 6 and figure 7 presented outline the results of various trials conducted during the training of a model, with a specific focus on tuning the learning rate and its impact on validation accuracy. The learning rate schedule appears to follow a dynamic adjustment mechanism, allowing for fine-tuning of the model's parameters over the course of the training process. As shown in the table, the learning rate varies across trials, with the highest validation accuracy achieved during Trial 4 at 99.44%, corresponding to a learning rate of $6.5451 \times 10^{-5}$. This suggests that during this trial, the model reached an optimal learning rate, which enabled effective training and allowed it to converge without falling into local minima. The results highlight how the choice of learning rate plays a crucial role in balancing the model's ability to generalize and improve performance during training.

*Table 6: Validation Accuracy and Learning Rate across Trials using dataset 2*

| Trail | Learning rate | Validation Accuracy % |
|---|---|---|
| 1 | 9.7553E-05 | 98.12 |
| 2 | 9.0451E-05 | 99.09 |
| 3 | 7.9389E-05 | 99.37 |
| 4 | 6.5451E-05 | 99.44 |
| 5 | 5.0000E-05 | 98.99 |
| 6 | 3.4549E-05 | 98.85 |
| 7 | 2.0611E-05 | 98.99 |
| 8 | 9.5492E-05 | 98.26 |
| 9 | 2.4472E-05 | 98.85 |
| 10 | 1.0000E-06 | 98.24 |

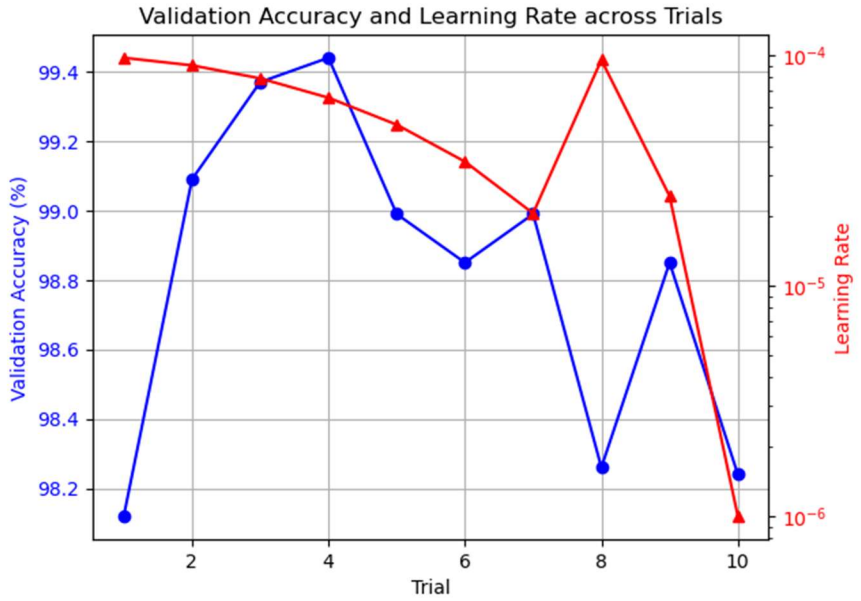


*Figure 7: Validation Accuracy and Learning Rate across Trials using dataset 2*

Throughout the trials, validation accuracy remains consistently high, with values ranging from 98.12% in Trial 1 to 99.44% in Trial 4, before gradually decreasing to 98.24% by Trial 10. The use of an appropriate learning rate likely allowed the model to avoid overfitting and converge effectively. For instance, the learning rate in Trial 5 ($5.0000 \times 10^{-5}$) maintained high validation accuracy at 98.99%, suggesting that the model still benefited from an adequately tuned rate, despite the slightly reduced performance compared to the peak observed in Trial 4. Interestingly, Trial 8 shows a significant spike in learning rate ($9.5492\times 10^{-5}$), which coincides with a drop in validation accuracy

to 98.26%. This suggests that the increased learning rate may have been too aggressive for the model, resulting in suboptimal weight adjustments and preventing further improvement in performance. Similarly, Trial 10, where the learning rate was reduced to $(1.0000 \times 10^{-6})$, demonstrated one of the lowest validation accuracies (98.24%), indicating that an overly small learning rate slowed down the convergence process and led to diminished results. Overall, the table 6 and figure 7 underscore the importance of finding a balance in learning rate tuning during training. Learning rates that are too high or too low can negatively impact performance, either by overshooting optimal weight values or slowing down convergence. By trialing different learning rates, the model achieves robust performance with consistently high validation accuracy, reflecting the effectiveness of the learning rate adjustment schedule employed during training. The dynamic adjustment approach likely played a significant role in enhancing feature extraction and stabilizing the training process across different trials.

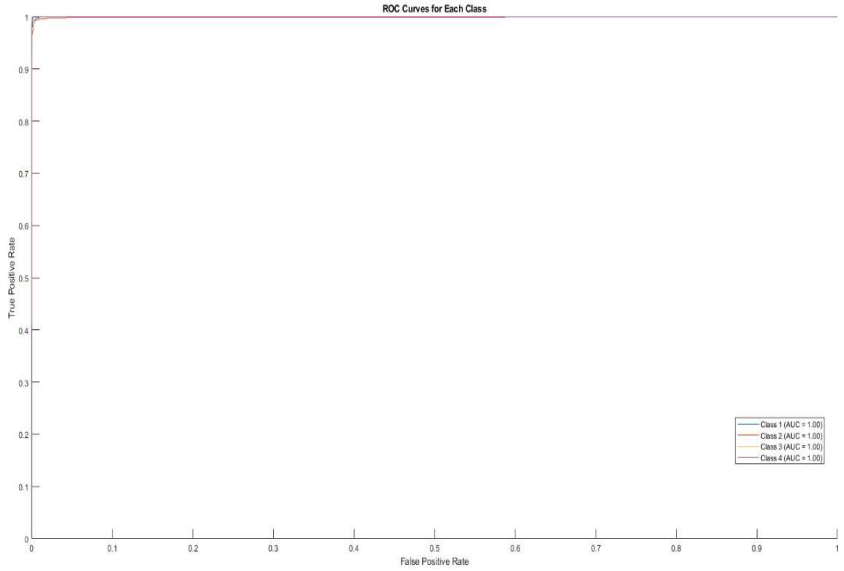


*Figure 8: ROC Curve Based On Proposed Model In Dataset 2*

*Table 7: Performance Metrics Based On Proposed Model In Dataset 2*

| Class | Accuracy | Precision | Recall | F1-Score | AUC | Specificity | Dice Coefficient |
|---|---|---|---|---|---|---|---|
| Glioma Tumor | 0.9972 | 0.9988 | 0.9915 | 0.9951 | 1.00 | 0.9995 | 0.9951 |
| Meningioma Tumor | 0.9962 | 0.9915 | 0.9951 | 0.9933 | 1.00 | 0.9966 | 0.9933 |
| No Tumor | 0.9997 | 1.0000 | 0.9975 | 0.9987 | 1.00 | 1.0000 | 0.9987 |
| Pituitary Tumor | 0.9990 | 0.9976 | 0.9988 | 0.9982 | 1.00 | 0.9990 | 0.9982 |
| ***Average*** | ***0.9980*** | ***0.9970*** | ***0.9957*** | ***0.9963*** | ***1.00*** | ***0.9988*** | ***0.9963*** |

The table 7 presents the performance metrics of a classification model across four classes: Glioma Tumor, Meningioma Tumor, No Tumor, and Pituitary Tumor. The metrics evaluated include Accuracy, Precision, Recall, F1-Score, AUC (Area Under the Curve), Specificity, and Dice Coefficient. These metrics are critical in understanding the performance of the model in terms of correctly classifying each type of tumor and distinguishing between tumor and non-tumor classes. Across all classes, the accuracy remains very high, ranging from 0.9962 for Meningioma

Tumor to 0.9997 for No Tumor. This indicates that the model correctly classified the majority of samples, regardless of class. Precision scores are also remarkably high, ranging from 0.9915 (Meningioma Tumor) to a perfect score of 1.0000 (No Tumor). High precision means that when the model predicts a certain class, it is almost always correct. Recall measures the model's ability to identify true positive cases. The scores vary from 0.9915 (Glioma Tumor) to 0.9988 (Pituitary Tumor). The high recall values indicate that the model is effective in capturing the positive cases across all classes. The F1-Score, which is the harmonic mean of precision and recall, is high across the board, with the lowest score being 0.9933 (Meningioma Tumor) and the highest being 0.9987 (No Tumor). This reflects the model's balanced performance between precision and recall. The AUC is perfect (1.00) for all classes, meaning the model excels at distinguishing between the positive class and the negative class in all instances as shown in figure 8. A perfect AUC score suggests that the model is very well-calibrated and able to differentiate between tumor types and the absence of a tumor. Specificity measures how well the model identifies true negatives. The values range from 0.9966 (Meningioma Tumor) to a perfect score of 1.0000 (No Tumor). This implies that the model is highly effective in avoiding false positives. The Dice Coefficient, which is a similarity measure, has high values across all classes, indicating strong overlap between the predicted and true classifications. The lowest value is 0.9933 (Meningioma Tumor), and the highest is 0.9987 (No Tumor), showing that the model predictions are highly accurate. The average metrics for the model across all classes are very strong, with an average accuracy of 0.9980, precision of 0.9970, recall of 0.9957, F1-Score of 0.9963, AUC of 1.00, specificity of 0.9988, and Dice Coefficient of 0.9963. This indicates the model performs exceptionally well in classifying tumor types and distinguishing between tumor and non-tumor cases. No Tumor class achieves the highest performance with perfect precision, AUC, and specificity, reflecting the model's strong ability to distinguish between healthy (non-tumor) and tumor cases. Meningioma Tumor shows slightly lower metrics compared to other classes, with the lowest recall and Dice Coefficient values. This suggests that the model might struggle slightly more with this particular tumor class, though performance is still excellent. Glioma Tumor and Pituitary Tumor both exhibit high performance across all metrics, suggesting that the model is highly reliable in identifying these tumor types.

*Explainability Analysis:* Figure 9 shows that an Ependymoma T1 was misclassified as a Schwannoma T1 by the model. Figure 9a shows the T1-weighted scan showing the cross-section of the brain, which contains an Ependymoma tumor. T1-weighted images provide clear anatomical details, especially for soft tissues. The tumor is present, but the model incorrectly identified it as a Schwannoma, another type of brain tumor with different characteristics. The distinction between these tumors is subtle and challenging because their appearances in certain imaging modalities may overlap. The occlusion sensitivity map, figure 9b, shows which parts of the image were most influential in the model's decision. In this case, the red and yellow regions indicate the areas the model focused on while making the misclassification. In the frontal brain region, the model has found patterns or features it considered important for its classification decision. However, these highlighted areas likely resemble characteristics of a Schwannoma rather than an Ependymoma, causing the misclassification. This suggests that the model incorrectly over-prioritized features in these areas, likely because certain characteristics, such as tissue density or signal intensity, were incorrectly interpreted as indicative of a Schwannoma. The gradient attribution map shown in figure 9c highlights which specific pixels influenced the model's classification the most. The bright red and yellow regions, particularly in the upper frontal areas of the brain, were heavily weighted in the model's decision. These highlighted areas represent features the model used to conclude that the image was of a Schwannoma, when in fact, it is an Ependymoma. This map shows that the model placed significant weight on features from regions where the two tumor types may have similar visual characteristics, leading to a confusion between the two.

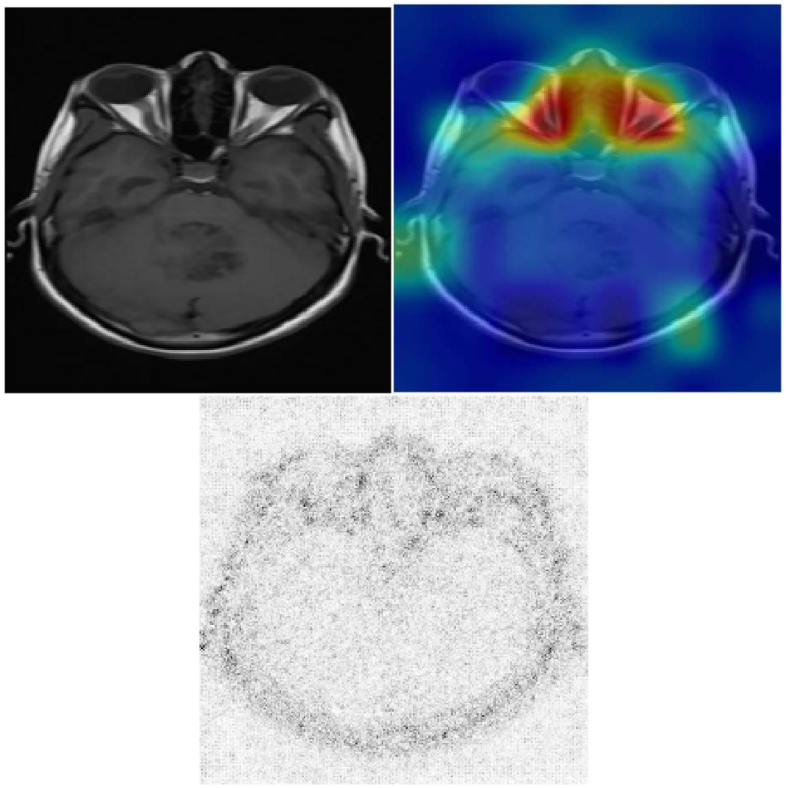

(a) (b) (c)

*Figure 9: Ependimoma T1 Classified As Schwannoma T1 Of Dataset 1 (A) Original Image (B) Occlusion Sensitivity (C) The Gradient Attribution*

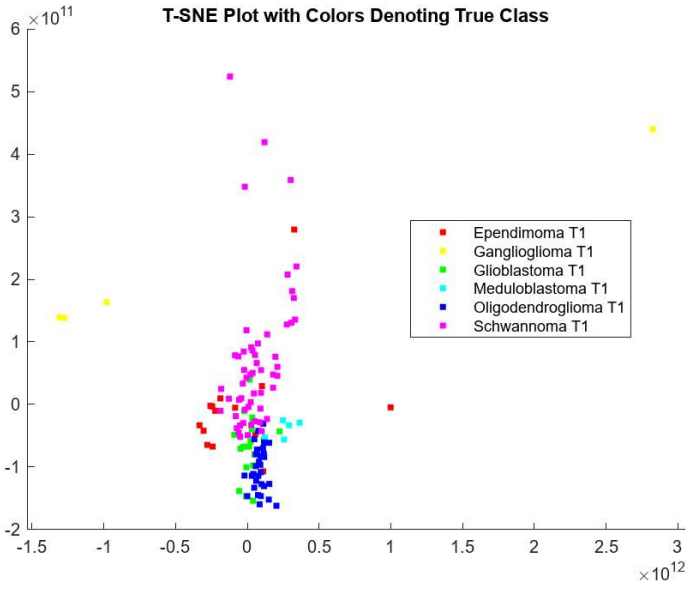


*Figure 10: T-SNE Plot With Colors Denoting True Class For Dataset 1*

The t-SNE plot, figure 10, illustrates the distribution of various tumor classes in a reduced two-dimensional space, aiming to visually discern the separability and clustering of these classes based on their intrinsic features. Each point on the plot corresponds to an individual tumor sample,

with colors denoting the specific tumor type, as per the legend: Ependimoma (red), Ganglioglioma (yellow), Glioblastoma (green), Medulloblastoma (cyan), Oligodendroglioma (blue), and Schwannoma (magenta). The t-SNE algorithm is particularly effective at preserving local structures in the data, meaning that points that are close in the original high-dimensional space are likely to be close in the two-dimensional projection. This property is evident in the plot, where distinct clusters of similarly colored points suggest that the t-SNE has captured the underlying feature similarities within each tumor class. For instance, the Oligodendroglioma (blue) and Schwannoma (magenta) classes exhibit relatively tight clustering, indicating that the features defining these tumor types are more homogeneous and distinct from others. Conversely, the spread and overlap among some classes, such as the slight intermingling between Ependimoma (red) and other classes, suggest that there might be shared features or potential ambiguity in classification based on the chosen features. This overlap could imply either a biological similarity between these tumor types or limitations in the feature set used, which may not fully capture the distinctions necessary for clear separation. Moreover, the vertical dispersion of the Schwannoma (magenta) points is notable, potentially indicating a broader variability within this class or the presence of subtypes with distinct characteristics that t-SNE is highlighting. The plot's structure, with most data points concentrated near the center and a few outliers, might reflect the complexity of the data, where most samples are similar, but certain instances possess unique features that distinguish them from the rest.

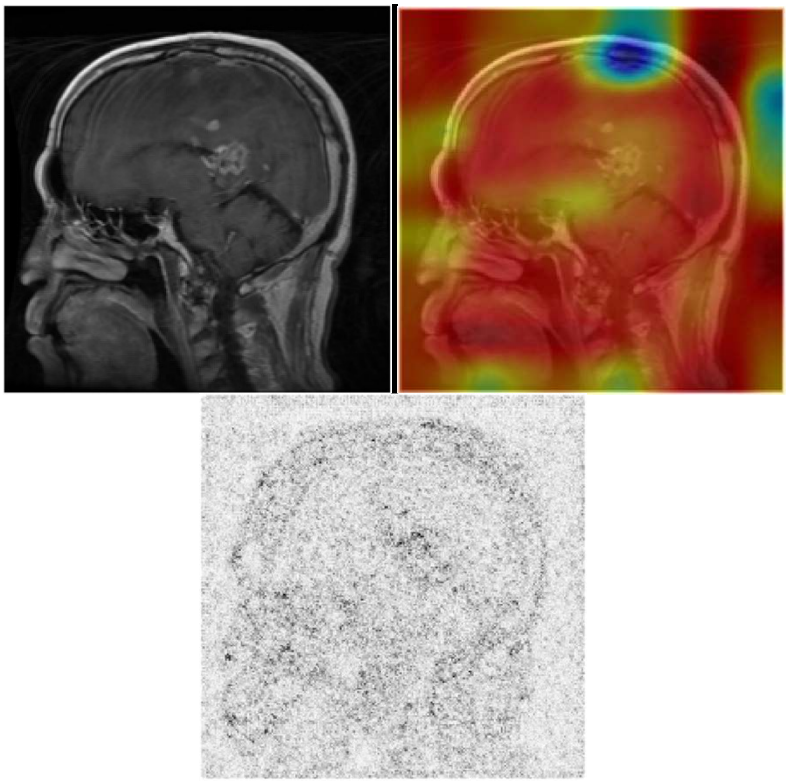

(a) (b) (c)

*Figure 11: Glioma Tumor Classified As Meningioma Tumor Of Dataset 2 (A) Original Image (B) Occlusion Sensitivity (C) The Gradient Attribution*

In Figures 11, 12, and 13, a deep learning model is applied to classify different types of brain tumors based on MRI scans. The figures visualize the misclassification of glioma, meningioma, and pituitary tumors, using two interpretability techniques: occlusion sensitivity and gradient attribution. These visualization techniques provide insights into why the model made specific classification errors by highlighting the regions in the MRI scans that influenced the model's predictions.

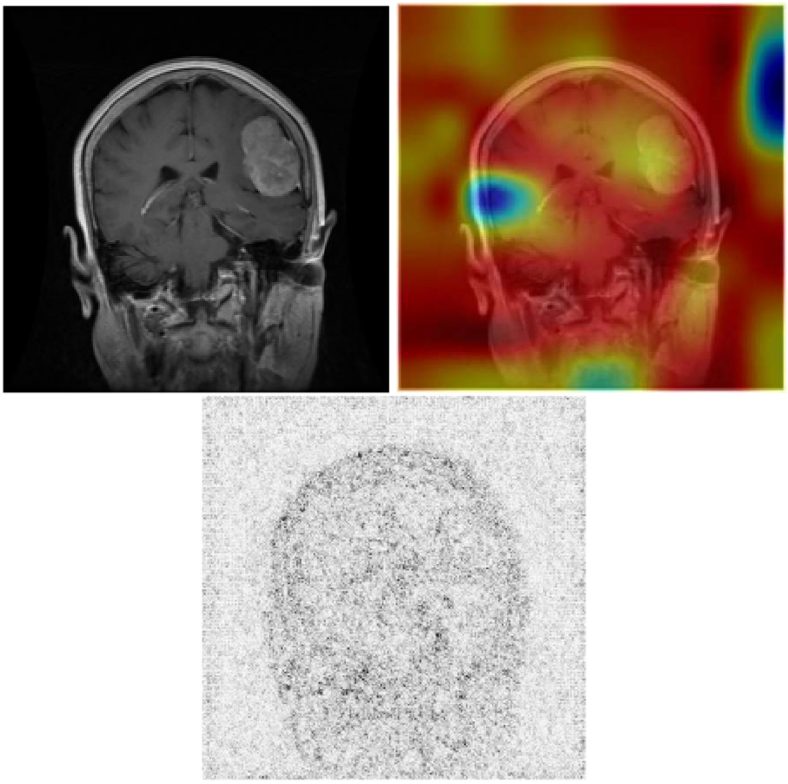

(a) (b) (c)

*Figure 12: Meningioma Tumor Classified As Glioma Tumor Of Dataset 2 (A) Original Image (B) Occlusion Sensitivity (C) The Gradient Attribution*

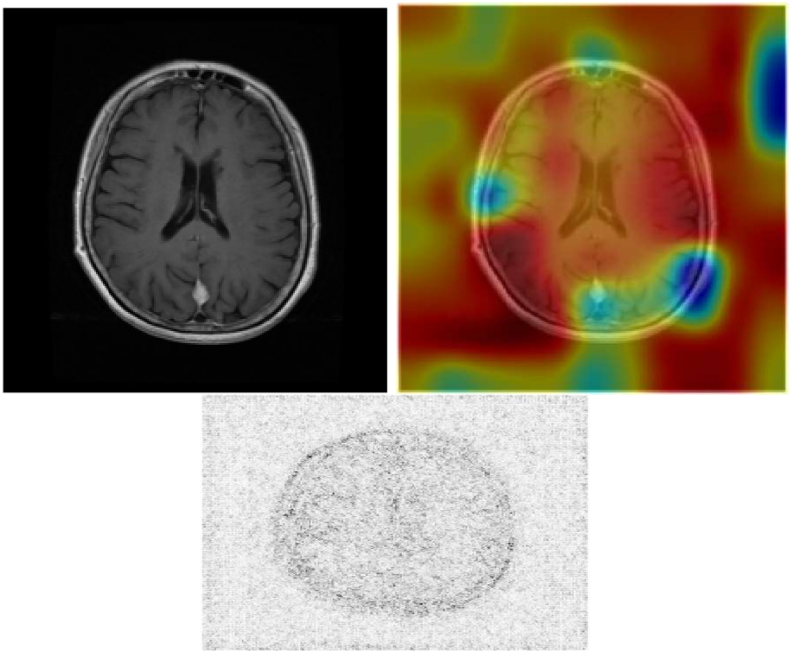

(a) (b) (c)

*Figure 13: Pituitary Tumor Classified As Meningioma Tumor Of Dataset 2 (A) Original Image (B) Occlusion Sensitivity (C) The Gradient Attribution*

In Figure 11, the original MRI image shows a glioma tumor, but the model incorrectly classified it as a meningioma. The occlusion sensitivity map in panel Figure 11b shows how different regions of the brain contributed to this misclassification, with red areas indicating strong influence on the decision to classify the tumor as a meningioma. The gradient attribution map in panel Figure 11c highlights the pixel-wise contributions to the decision, showing that several parts of the brain image influenced the model, but not necessarily in a biologically relevant way. This suggests that the model may have focused on irrelevant areas, leading to the incorrect classification.

Figure 12 depicts a case where a meningioma tumor was misclassified as a glioma. The occlusion sensitivity, shown in Figure 12b, map demonstrates that the model assigned significant weight to regions near the tumor but misinterpreted their importance, likely confusing features of the meningioma with those of glioma. In the gradient attribution map, shown in Figure 12c, the influence of individual pixels is dispersed, which might indicate that the model did not capture the salient features of the meningioma that would have led to a correct classification. This reflects a possible issue with the model's ability to differentiate between these two tumor types based on spatial or textural differences in the scan.

Finally, Figure 13 illustrates the misclassification of a pituitary tumor as a meningioma. The occlusion sensitivity map, shown in Figure 13b, reveals that regions distant from the tumor were emphasized, suggesting the model might have used non-discriminative areas of the brain scan to make its prediction. The gradient attribution, shown in Figure 13c, map further confirms this, as the pixel influences are scattered across the scan, without clearly focusing on the tumor region. This misclassification could indicate that the model is not sufficiently specialized to distinguish between pituitary and meningioma tumors, perhaps due to overlapping features or insufficient training data for certain tumor types.

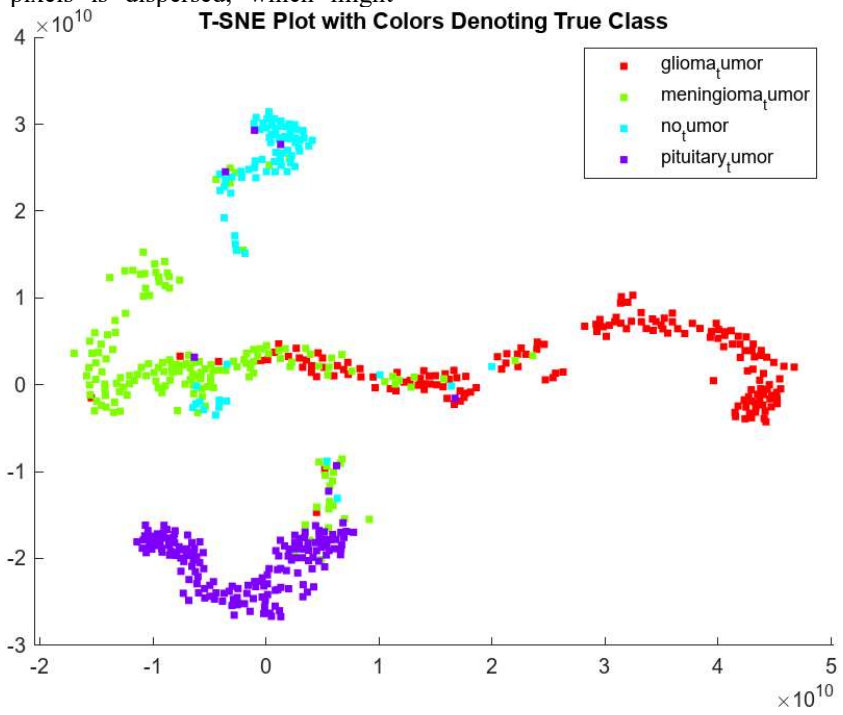


*Figure 14: T-SNE Plot With Colors Denoting True Class For Dataset 2*

The figure 14 shows a t SNE plot used to display datasets in a simpler two-dimensional form. In this plot of t SNE analysis, for brain tumors and non-tumor samples are color coded to represent glioma tumors (red) meningioma tumors (green) no tumors (cyan) and pituitary tumors (purple).The t SNE algorithm groups together data points with similarities to each other which helps in analyzing how distinct the different classes are, in the feature space learned by a model. The visualization shows groupings representing various types of tumors. The red cluster representing glioma tumors stands out in the area suggesting that these samples have

unique characteristics that can be easily differentiated from other classes. The pituitary tumors (shown in purple on the plot) display a segregation, in the bottom left area of the graph which implies that this specific tumor category possesses unique traits that distinguish it from other types of tumors recognized by the model. However, the meningioma tumors (depicted in green) seem to overlap with both glioma tumors and samples without any tumor (depicted in cyan). This suggests a situation where the model might get confused as characteristics could resemble those of both glioma and normal brain tissues – potentially leading to misclassification errors. The classes overlap implies that the models learned feature representations for meningiomas are not completely distinct and could lead to classification errors as shown in figures 11 to 13. The cyan samples without tumors are scattered throughout the plot with some closeness, to the meningiomas samples which suggests that normal brain scans may show similarities to features seen in meningiomas cases. This might be the reason why the system sometimes finds it challenging to differentiate between brain tissues and noncancerous tumors such, as meningothelial ones.

***Potential benefits of explainability in high-stakes medical contexts.***

In high-stakes medical contexts, such as brain tumor detection and classification, explainability is vital for clinicians to understand model decisions, confirm or challenge predictions, and ultimately trust the technology in clinical settings. Here are some specific benefits and aspects highlighted by the model's explainability features in the context of brain tumor detection:

*1. Enhanced Transparency and Trust in AI Predictions*

- Sensitivity maps, such as occlusion sensitivity and gradient attribution, reveal which areas of an MRI image contributed most to a model's classification decision.
- This transparency helps clinicians see why the model arrived at a certain classification, potentially highlighting the regions it deems similar to known tumor patterns. If a misclassification occurs, clinicians can assess whether the model may have focused on irrelevant regions or misinterpreted certain features, as seen when the model misclassified glioma as meningioma in Figure 11.

*2. Insight into Model Limitations and Areas for Improvement*

- Explainability maps can help identify the model's weaknesses, especially where certain tumor types may share visual characteristics that lead to confusion. For example, in Figure 9, the model mistook an Ependymoma for a Schwannoma due to overlapping visual features in the T1-weighted scan.
- By pinpointing these confusions, sensitivity maps enable refinement of feature selection or model retraining in specific areas, such as including more nuanced training data for look-alike tumor types.

*3. Supporting Clinical Decision-Making and Reducing Diagnostic Uncertainty*

- Explainability maps provide additional visual confirmation, helping radiologists to either validate the AI's prediction or investigate further if the highlighted regions do not match expected patterns.
- This capability reduces uncertainty, particularly in complex cases where tumor boundaries are not clearly defined or where multiple tumor types may appear visually similar. For example, in Figure 12, the model's focus on regions near the meningioma tumor led to its misclassification as a glioma, prompting clinicians to consider additional diagnostic imaging or clinical evaluation to verify.

*4. Understanding Tumor-Specific Characteristics for Improved Feature Selection*

- Sensitivity maps highlight which image features, such as tissue density, signal intensity, or texture, were critical to the model's decision, especially in complex tumors.
- This information is beneficial in refining the model's focus on the most diagnostic features and training it to prioritize clinically relevant tumor characteristics. In Figure 13, where a pituitary tumor was misclassified as meningioma, the sensitivity map suggested that certain non-discriminative regions were erroneously prioritized, signaling a need to adjust feature weighting or model tuning.

*5. Minimizing Misdiagnosis and Enhancing Patient Safety*

- Explainable AI models help reduce the risk of misdiagnosis, as they allow radiologists to interpret why a model may have leaned towards a certain classification. If a model's

prediction does not align with clinical intuition, explainability maps encourage clinicians to seek additional tests or consider alternate diagnoses.

- In Figure 10, the t-SNE plot shows close clustering between Ependymoma and other classes, suggesting ambiguity in the model's learned features for these tumor types. Awareness of this limitation can prompt clinicians to exercise caution in diagnosis, reducing potential misclassification risks.

*6. Adaptability and Continuous Model Improvement*

- Explainability tools allow researchers and clinicians to identify systematic biases in model behavior, such as over-prioritizing non-relevant regions or lacking focus on key tumor characteristics.
- These insights facilitate continuous model refinement and adaptation, especially critical as new imaging techniques or tumor types are introduced into clinical practice.

**Comparison with state of art models**

*Table 8 Comparison With State Of Art Models With The Proposed Model*

| Reference | Model | Accuracy |
|---|---|---|
| [39] | region augmentation and partition | 91.28 |
| [40] | CNN | 91.43 |
| [41] | Capsule networks | 90.89 |
| [42] | CNN + genetic algorithms | 94.2 |
| [43] | CNN+ fine-tuning | 94.82 |
| [44] | CNN | 95.23 ± 0.6 |
| | Proposed Method<br>CNN+ Quantum Inspired concepts | 99.80 |

The table 8 compares the performance of various models in terms of accuracy for a particular task. The proposed Quantum-Inspired Convolutional Neural Network (QCNN) achieves significantly higher accuracy (99.80%) than competing state-of-the-art models. This remarkable performance improvement can be attributed to several unique aspects of the quantum-inspired approach that enhance both feature extraction and optimization. Traditional CNN models, like the ones in [40] (91.43%) and [44] (95.23%), rely heavily on classical convolution operations to identify features in images. While these methods have proven effective, they may miss subtle patterns or complex feature relationships in highly dimensional data. The QCNN leverages principles of quantum mechanics, such as superposition and entanglement, allowing it to analyze multiple feature combinations simultaneously. This holistic approach improves the network's ability to extract and represent complex features, which is particularly advantageous for nuanced tasks like distinguishing between brain tumor types. This capability enhances precision, distinguishing the QCNN from models with limited feature extraction strategies. Capsule networks [41] (90.89%) and CNN models enhanced with genetic algorithms [42] (94.2%) incorporate advanced optimization techniques to improve convergence. However, these approaches may still struggle with local minima in the high-dimensional search space, limiting their optimization effectiveness. The QCNN employs quantum-inspired optimization techniques that mimic quantum tunneling, which can help it avoid local minima by effectively "jumping" over suboptimal solutions. This quantum-inspired characteristic aids in achieving a global optimum and refining accuracy to an unprecedented level, unlike models using classical optimization techniques, which may converge to less optimal solutions. Fine-tuning methods, as in [43] (94.82%), improve a model's adaptability across datasets but may still lead to overfitting, particularly in large CNN architectures. Region augmentation [39] (91.28%) tries to mitigate overfitting by exposing the model to diverse image sections, yet it doesn't fully address overfitting in feature-dense tasks. The QCNN's quantum-inspired components increase the model's ability to generalize by effectively balancing the exploration and exploitation phases during learning. This balance enables the QCNN to capture a more robust set of features across varying data distributions, reducing the risk of overfitting and improving reliability on diverse MRI data. Standard CNN architectures require extensive computational resources for large, complex datasets, as they process each convolution layer sequentially, often

leading to higher costs and time constraints. Although some models use genetic algorithms or capsule networks to improve efficiency, they still require significant resources for optimal performance. The quantum-inspired framework in the QCNN enables parallelism, which decreases computational requirements while maintaining high performance. This efficiency allows the QCNN to outperform other models without proportionally increasing resource demands, making it a more viable option for clinical applications where real-time processing is essential. Hence, the quantum-inspired aspects of the QCNN, such as advanced feature extraction, optimized convergence, improved generalization, and computational efficiency, contribute significantly to its superior performance. These unique characteristics set the QCNN apart from traditional CNN and advanced models, providing a substantial accuracy advantage while reducing operational complexity, making it an optimal solution for high-stakes, nuanced tasks like brain tumor classification.

## 5. CONCLUSION

This study presents a Quantum-Inspired Convolutional Neural Network (QCNN) represents a breakthrough in brain tumor detection by integrating quantum computing principles with the traditional CNN framework. This combined approach has demonstrated high precision and recall across various tumor types, enhances feature extraction and classification accuracy, positioning it as a promising tool for clinical application in tumor diagnosis. By achieving a high degree of accuracy and adaptability, the model offers a promising tool for clinical applications where timely and accurate diagnoses are critical. QCNN's effective differentiation between healthy and abnormal brain tissues makes it valuable for identifying different tumor types, potentially aiding in treatment planning and patient care. Furthermore, the model's application of a cosine annealing learning rate schedule contributed significantly to its optimized performance, helping it navigate parameter spaces efficiently and avoid overfitting. This enhancement underscores QCNN's advancement over traditional CNNs in feature extraction, classification accuracy, and operational efficiency. Future studies could explore QCNN's applicability across broader medical imaging domains, evaluating its performance on other challenging datasets and investigating the potential to incorporate additional quantum-inspired features. By refining the model further, there is potential for even broader application across critical diagnostic contexts.

## REFERENCES

[1] Delaidelli A, Moiraghi A. Recent Advances in the Diagnosis and Treatment of Brain Tumors. Brain Sciences. 2024; 14(3):224. https://doi.org/10.3390/brainsci14030224.

[2] David N Louis, Arie Perry, Pieter Wesseling, Daniel J Brat, Ian A Cree, Dominique Figarella-Branger, Cynthia Hawkins, H K Ng, Stefan M Pfister, Guido Reifenberger, Riccardo Soffietti, Andreas von Deimling, David W Ellison, The 2021 WHO Classification of Tumors of the Central Nervous System: a summary, *Neuro-Oncology*, Volume 23, Issue 8, August 2021, Pages 1231–1251, https://doi.org/10.1093/neuonc/noab106

[3] Aldape, K., Brindle, K.M., Chesler, L. *et al.* Challenges to curing primary brain tumours. *Nat Rev Clin Oncol* **16**, 509–520 (2019). https://doi.org/10.1038/s41571-019-0177-5

[4] Birzu C, French P, Caccese M, Cerretti G, Idbaih A, Zagonel V, Lombardi G. Recurrent Glioblastoma: From Molecular Landscape to New Treatment Perspectives. *Cancers*. 2021; 13(1):47. https://doi.org/10.3390/cancers13010047

[5] Villanueva-Meyer JE, Mabray MC, Cha S. Current Clinical Brain Tumor Imaging. Neurosurgery. 2017 Sep 1;81(3):397-415. doi: 10.1093/neuros/nyx103. PMID: 28486641; PMCID: PMC5581219.

[6] Martucci M, Russo R, Schimperna F, D'Apolito G, Panfili M, Grimaldi A, Perna A, Ferranti AM, Varcasia G, Giordano C, Gaudino S. Magnetic Resonance Imaging of Primary Adult Brain Tumors: State of the Art and Future Perspectives. Biomedicines. 2023 Jan 26;11(2):364. doi: 10.3390/biomedicines11020364. PMID: 36830900; PMCID: PMC9953338.

[7] Abdusalomov AB, Mukhiddinov M, Whangbo TK. Brain Tumor Detection Based on Deep Learning Approaches and Magnetic Resonance Imaging. Cancers (Basel). 2023 Aug 18;15(16):4172. doi: 10.3390/cancers15164172. PMID: 37627200; PMCID: PMC10453020.

[8] Saeedi, S., Rezayi, S., Keshavarz, H. *et al.* MRI-based brain tumor detection using convolutional deep learning methods and

chosen machine learning techniques. *BMC Med Inform Decis Mak* **23**, 16 (2023). https://doi.org/10.1186/s12911-023-02114-6.

[9] Mathivanan, S.K., Sonaimuthu, S., Murugesan, S. *et al.* Employing deep learning and transfer learning for accurate brain tumor detection. *Sci Rep* **14**, 7232 (2024). https://doi.org/10.1038/s41598-024-57970-7

[10] Z. Yan et al., "HD-CNN: Hierarchical Deep Convolutional Neural Networks for Large Scale Visual Recognition," 2015 IEEE International Conference on Computer Vision (ICCV), Santiago, Chile, 2015, pp. 2740-2748, doi: 10.1109/ICCV.2015.314

[11] Roy, Deboleena, Priyadarshini Panda, and Kaushik Roy. "Tree-CNN: a hierarchical deep convolutional neural network for incremental learning." Neural networks 121 (2020): 148-160.

[12] Alzubaidi, L., Zhang, J., Humaidi, A.J. *et al.* Review of deep learning: concepts, CNN architectures, challenges, applications, future directions. *J Big Data* **8**, 53 (2021). https://doi.org/10.1186/s40537-021-00444-8

[13] Zhang H, Qie Y. Applying Deep Learning to Medical Imaging: A Review. *Applied Sciences*. 2023; 13(18):10521. https://doi.org/10.3390/app131810521

[14] Sarvamangala, D.R., Kulkarni, R.V. Convolutional neural networks in medical image understanding: a survey. Evol. Intel. 15, 1–22 (2022). https://doi.org/10.1007/s12065-020-00540-3

[15] Ilesanmi, A. E., Ilesanmi, T. O., & Ajayi, B. O. (2024). Reviewing 3D convolutional neural network approaches for medical image segmentation. Heliyon, 10(6), e27398. https://doi.org/10.1016/j.heliyon.2024.e27398

[16] Konar, D., Bhattacharyya, S., Dey, S., & Panigrahi, B. K. (2022). Optimized activation for quantum-inspired self-supervised neural network based fully automated brain lesion segmentation. Applied Intelligence, 52(13), 15643–15672. https://doi.org/10.1007/s10489-021-03108-5.

[17] Yang, Z., & Zhang, X. (2020). Entanglement-based quantum deep learning. New Journal of Physics, 22(3), 033041. https://doi.org/10.1088/1367-2630/ab7598.

[18] Chen, G., Chen, Q., Long, S., Zhu, W., Yuan, Z., & Wu, Y. (2022). Quantum convolutional neural network for image classification. Pattern Analysis and Applications, 26(2), 655–667. https://doi.org/10.1007/s10044-022-01113-z

[19] Ajlouni, N., Özyavaş, A., Takaoğlu, M., Takaoğlu, F., & Ajlouni, F. (2023). Medical image diagnosis based on adaptive Hybrid Quantum CNN. BMC Medical Imaging, 23(1). https://doi.org/10.1186/s12880-023-01084-5.

[20] Valdez, F., & Melin, P. (2022). A review on quantum computing and deep learning algorithms and their applications. Soft Computing, 27(18), 13217–13236. https://doi.org/10.1007/s00500-022-07037-4

[21] Nodirov, J., Abdusalomov, A. B., & Whangbo, T. K. (2022). Attention 3D U-Net with Multiple Skip Connections for Segmentation of Brain Tumor Images. Sensors, 22(17), 6501. https://doi.org/10.3390/s22176501.

[22] Abd-Ellah, M. K., Awad, A. I., Khalaf, A. A., & Hamed, H. F. (2019). A review on brain tumor diagnosis from MRI images: Practical implications, key achievements, and lessons learned. Magnetic Resonance Imaging, 61, 300–318. https://doi.org/10.1016/j.mri.2019.05.028.

[23] Yushkevich, P. A., Gao, Y., & Gerig, G. (2016). ITK-SNAP: An interactive tool for semi-automatic segmentation of multi-modality biomedical images. In Proceedings of the 2016 38th Annual International Conference of the IEEE Engineering in Medicine and Biology Society (EMBC), Orlando, FL, USA, 16–20 August 2016; pp. 3342–3345. https://doi.org/10.1109/embc.2016.7591443.

[24] Araújo, T., Aresta, G., Castro, E., Rouco, J., Aguiar, P., Eloy, C., Polónia, A., & Campilho, A. (2017). Classification of breast cancer histology images using Convolutional Neural Networks. PLoS ONE, 12(6), e0177544. https://doi.org/10.1371/journal.pone.0177544.

[25] Çinar, A., & Yildirim, M. (2020). Detection of tumors on brain MRI images using the hybrid convolutional neural network architecture. Medical Hypotheses, 139, 109684. https://doi.org/10.1016/j.mehy.2020.109684.

[26] Krizhevsky, A., Sutskever, I., & Hinton, G. E. (2017). ImageNet classification with deep convolutional neural networks. Communications of the ACM, 60(6), 84–90. https://doi.org/10.1145/3065386.

[27] Szegedy, C., Liu, N. W., Jia, N. Y., Sermanet, P., Reed, S., Anguelov, D., Erhan, D., Vanhoucke, V., & Rabinovich, A. (2015). Going deeper with convolutions. In: Proceedings of the IEEE Conference on Computer Vision and Pattern Recognition; 2015. P. 1–9. https://doi.org/10.1109/cvpr.2015.7298594.

[28] He, K., Zhang, X., Ren, S., & Sun, J. (2016b). Deep Residual Learning for Image Recognition. In: Proceedings of the IEEE Conference on Computer Vision and Pattern Recognition; 2016. P. 770–8. https://doi.org/10.1109/cvpr.2016.90.

[29] Tan, C., Sun, F., Kong, T., Zhang, W., Yang, C., & Liu, C. (2018). A survey on Deep transfer learning. In Lecture notes in computer science (pp. 270–279). https://doi.org/10.1007/978-3-030-01424-7_27.

[30] Deng, J., Dong, W., Socher, R., Li, L., Li, N. K., & Fei-Fei, N. L. (2009). ImageNet: A large-scale hierarchical image database. 2009 IEEE Conference on Computer Vision and Pattern Recognition. https://doi.org/10.1109/cvpr.2009.5206848.

[31] Raghu, M., Zhang, C., Kleinberg, J. M., & Bengio, S. (2019). Transfusion: Understanding Transfer learning for medical imaging. Neural Information Processing Systems, 32, 3342–3352. https://papers.nips.cc/paper/2019/file/eb1e78328c46506b46a4ac4a1e378b91-Paper.pdf.

[32] Pham, T. N., Van Tran, L., & Dao, S. V. T. (2020). Early disease classification of mango leaves using Feed-Forward neural network and hybrid metaheuristic feature selection. IEEE Access, 8, 189960–189973. https://doi.org/10.1109/access.2020.3031914.

[33] Gonaygunta, H., Maturi, M. H., Nadella, G. S., Meduri, K., & Satish, S. (2024). Quantum Machine Learning: Exploring quantum algorithms for enhancing deep learning models. International Journal of Advanced Engineering Research and Science, 11(5), 35–41. https://doi.org/10.22161/ijaers.115.5.

[34] Shi, S., Wang, Z., Cui, G. et al. Quantum-inspired complex convolutional neural networks. Appl Intell 52, 17912–17921 (2022). https://doi.org/10.1007/s10489-022-03525-0

[35] Fan, Z., Zhang, J., Zhang, P., Lin, Q., & Gao, H. (2024). Quantum-Inspired Neural Network with Runge-Kutta Method. Proceedings of the AAAI Conference on Artificial Intelligence, 38(16), 17977–17984. https://doi.org/10.1609/aaai.v38i16.29753.

[36] Huynh, Larry, et al. "Quantum-inspired machine learning: a survey." *arXiv preprint arXiv:2308.11269* (2023).

[37] Mishra, Nimish, et al. "Quantum machine learning: A review and current status." *Data Management, Analytics and Innovation: Proceedings of ICDMAI 2020, Volume 2* (2021): 101-145.

[38] Jun-Jie Zhang, Deyu Meng, Quantum-inspired analysis of neural network vulnerabilities: the role of conjugate variables in system attacks, National Science Review, Volume 11, Issue 9, September 2024, nwae141, https://doi.org/10.1093/nsr/nwae141

[39] Cheng, J., Huang, W., Cao, S., Yang, R., Yang, W., Yun, Z., Wang, Z., & Feng, Q. (2015). Enhanced performance of brain tumor classification via tumor region augmentation and partition. PLoS ONE, 10(10), e0140381. https://doi.org/10.1371/journal.pone.0140381.

[40] Paul, J. S., Plassard, A. J., Landman, B. A., & Fabbri, D. (2017). Deep learning for brain tumor classification. Proceedings of SPIE, the International Society for Optical Engineering/Proceedings of SPIE. https://doi.org/10.1117/12.2254195.

[41] P. Afshar, et al., "Capsule networks for brain tumor classification based on MRI images and course tumor boundaries," 2018. [Online]. Available:https://arxiv.org/abs/1811.00597.

[42] Anaraki, A. K., Ayati, M., & Kazemi, F. (2019). Magnetic resonance imaging-based brain tumor grades classification and grading via convolutional neural networks and genetic algorithms. Journal of Applied Biomedicine, 39(1), 63–74. https://doi.org/10.1016/j.bbe.2018.10.004.

[43] Swati, Z. N. K., Zhao, Q., Kabir, M., Ali, F., Ali, Z., Ahmed, S., & Lu, J. (2019). Brain tumor classification for MR images using transfer learning and fine-tuning. Computerized Medical Imaging and Graphics, 75, 34–46. https://doi.org/10.1016/j.compmedimag.2019.05.001.

[44] Talo, M., Yildirim, O., Baloglu, U. B., Aydin, G., & Acharya, U. R. (2019). Convolutional neural networks for multi-class brain disease detection using MRI images. Computerized Medical Imaging and Graphics, 78, 101673. https://doi.org/10.1016/j.compmedimag.2019.101673.

[45] B. H. Menze, A. Jakab, S. Bauer, J. Kalpathy-Cramer, K. Farahani, J. Kirby, et al. "The Multimodal Brain Tumor Image Segmentation Benchmark (BRATS)", IEEE Transactions on Medical Imaging 34(10), 1993-2024 (2015) DOI: 10.1109/TMI.2014.2377694.

[46] S. Bakas, H. Akbari, A. Sotiras, M. Bilello, M. Rozycki, J.S. Kirby, et al., "Advancing the Cancer Genome Atlas glioma MRI collections with expert segmentation labels and radiomic

features", Nature Scientific Data, 4:170117 (2017) DOI: 10.1038/sdata.2017.117

[47] S. Bakas, M. Reyes, A. Jakab, S. Bauer, M. Rempfler, A. Crimi, et al., "Identifying the Best Machine Learning Algorithms for Brain Tumor Segmentation, Progression Assessment, and Overall Survival Prediction in the BRATS Challenge", arXiv preprint arXiv:1811.02629 (2018)